Galileo disposal strategy: stability, chaos and predictability

Aaron Rosengren, Jérôme Daquin, Kleomenis Tsiganis, Elisa Maria Alessi, Florent Deleflie, Alessandro Rossi, Giovanni Valsecchi

▶ **To cite this version:**

Aaron Rosengren, Jérôme Daquin, Kleomenis Tsiganis, Elisa Maria Alessi, Florent Deleflie, et al.. Galileo disposal strategy: stability, chaos and predictability. Monthly Notices of the Royal Astronomical Society, 2017, 464 (4), pp.4063-4076. 10.1093/mnras/stw2459 . hal-02202236

HAL Id: hal-02202236
https://hal.science/hal-02202236

Submitted on 1 Aug 2022

HAL is a multi-disciplinary open access archive for the deposit and dissemination of scientific research documents, whether they are published or not. The documents may come from teaching and research institutions in France or abroad, or from public or private research centers.

L'archive ouverte pluridisciplinaire **HAL**, est destinée au dépôt et à la diffusion de documents scientifiques de niveau recherche, publiés ou non, émanant des établissements d'enseignement et de recherche français ou étrangers, des laboratoires publics ou privés.

Monthly Notices
of the
ROYAL ASTRONOMICAL SOCIETY

MNRAS **464,** 4063–4076 (2017)
Advance Access publication 2016 September 29

doi:10.1093/mnras/stw2459

Galileo disposal strategy: stability, chaos and predictability

Aaron J. Rosengren,[1,2]★ Jérôme Daquin,[3,4] Kleomenis Tsiganis,[2] Elisa Maria Alessi,[1] Florent Deleflie,[3] Alessandro Rossi[1] and Giovanni B. Valsecchi[1,5]

[1]*IFAC-CNR, Via Madonna del Piano 10, I-50019 Sesto Fiorentino (FI), Italy*
[2]*Department of Physics, Aristotle University of Thessaloniki, 54124 Thessaloniki, Greece*
[3]*IMCCE/Observatoire de Paris, Université Lille1, 1 Impasse de l'Observatoire, F-59000 Lille, France*
[4]*SPACE Research Centre, School of Mathematical and Geospatial Sciences, Royal Melbourne Institute of Technology (RMIT) University, Melbourne 3001, Australia*
[5]*IAPS-INAF, Via Fosso del Cavaliere 100, I-00133 Roma, Italy*

Accepted 2016 September 23. Received 2016 September 23; in original form 2015 December 17

ABSTRACT

Recent studies have shown that the medium-Earth orbit (MEO) region of the global navigation satellite systems is permeated by a devious network of lunisolar secular resonances, which can interact to produce chaotic and diffusive motions. The precarious state of the four navigation constellations, perched on the threshold of instability, makes it understandable why all past efforts to define stable graveyard orbits, especially in the case of Galileo, were bound to fail; the region is far too complex to allow for an adoption of the simple geosynchronous disposal strategy. We retrace one such recent attempt, funded by ESA's General Studies Programme in the frame of the GreenOPS initiative, that uses a systematic parametric approach and the straightforward maximum-eccentricity method to identify long-term-stable regions, suitable for graveyards, as well as large-scale excursions in eccentricity, which can be used for post-mission deorbiting of constellation satellites. We then apply our new results on the stunningly rich dynamical structure of the MEO region towards the analysis of these disposal strategies for Galileo, and discuss the practical implications of resonances and chaos in this regime. We outline how the identification of the hyperbolic and elliptic fixed points of the resonances near Galileo can lead to explicit criteria for defining optimal disposal strategies.

Key words: chaos – methods: analytical – methods: numerical – celestial mechanics – planets and satellites: dynamical evolution and stability – planets and satellites: general.

1 INTRODUCTION

The application of the mathematical tools and techniques of nonlinear dynamics has provided astronomers with a deeper understanding of the dynamical processes that have helped to shape the Solar system (Morbidelli 2002). Resonant phenomena connected with the commensurability of frequencies of interacting motions abound in celestial mechanics and have both dynamical and theoretical importance. A succession of remarkable features in the asteroid belt, known as the Kirkwood gaps, vividly illustrates the physical significance of resonances and chaos in real systems. Considerable impetus has been imparted over the past three decades to the study and understanding of this type of chaotic unpredictability and its manifestation in other astronomical problems.

With chaotic motions being a natural consequence of even the most simplest of systems, it may no longer be sensible to investigate the 'exact' trajectory of a celestial body (natural or artificial) in a given time interval (q.v. Zeebe 2015, and references therein). Far beyond the Lyapunov time, the characteristic time over which an orbit is said to remain predictable, it is not possible to reproduce the same time evolution if the system is chaotic, due to the exponential growth of uncertainties (in the initial state, mismodelling effects, numerical errors, etc.). The irregular and haphazard character of the chaotic path of a celestial body reflects a similar irregularity in the trajectories of stochastic systems, as if the former were influenced by a random perturbation even though, in fact, the motion is governed by purely deterministic dynamical equations. There is, however, an essential difference: 'classical (i.e. non-quantum mechanical) chaotic systems are not in any sense intrinsically random or unpredictable,' as John Barrow puts it, 'they merely possess extreme sensitivity to ignorance' (Barrow 2010). Despite the unpredictability of the path of a particular orbit, chaotic systems can exhibit statistical regularities, and have stable, predictable, long-term, average behaviours (Lichtenberg & Lieberman 1992; Meiss 1992). The lesson is that the time evolution of a chaotic system can only be described in statistical terms; one must study the statistical properties of ensembles of stochastic orbits (e.g. Laskar & Gastineau 2009; Zeebe 2015).

Our knowledge about the stability of the orbits of artificial Earth satellites is still incomplete. Despite over 50 years of space

★ E-mail: a.rosengren@ifac.cnr.it

© 2016 The Authors
Published by Oxford University Press on behalf of the Royal Astronomical Society

Downloaded from https://academic.oup.com/mnras/article/464/4/4063/2527864 by guest on 01 August 2022

activities, we know amazingly little about the dynamical environment occupied by artificial satellites and space debris. Strange as it may seem, we understand the structure and evolution of the, mostly invisible, trans-Neptunian belts of small bodies (q.v. Morbidelli 2002) far better than we understand that of the artificial bodies that orbit our terrestrial abode. Before these remnants of Solar system formation diverted the interests and energies of space-age astronomers, such astrodynamical problems had stood in the foremost rank of astronomical research work (Brouwer 1959). The kind of Newtonian determinism brought to bear during the 1960s has continued merrily along in astrodynamics, unheeding the fundamental discoveries of non-linear dynamics. Today, we take for granted the great power and scope of modern computers, treating them as the supreme intelligence imagined by Laplace, and the construction of increasingly more 'accurate' and grandiloquent dynamical models and simulation capabilities has become the central task of the field.

As long as our thought processes are limited along the inflexibilities of determinism, we will remain forever ignorant of the possible range and vagaries of chaos in Earth-satellite orbits. An understanding of these chaotic phenomena is of fundamental importance for all efforts to assess debris mitigation measures – efforts that may shed much light on the design and definition of optimal disposal strategies throughout all space regions (low-Earth orbits, medium-Earth orbits (MEOs), geostationary orbits, highly elliptical orbits, libration point orbits), taking into account orbital interaction and environmental evolution. In this context, there has been considerable recent interest in designing novel deorbiting or re-orbiting solutions for the MEO navigation satellites (qq.v. Alessi et al. 2016; Radtke et al. 2015; Sanchez, Yokoyama & Prado 2015, and references therein), since the operational constellations and recommended graveyard orbits have been found to be unstable (Chao 2000; Jenkin & Gick 2005).

The intent of this paper is to provide a case study on the European Galileo system that can be used as a reference for the other constellations, and to serve as a springboard for investigating new dynamical situations that may arise. We begin by reviewing our recent parametric numerical study on two end-of-life disposal strategies, based on the Laplacian paradigm, which investigates the role of the initial parameters of the disposal orbits (the semimajor axis, eccentricity, inclination, orientation phase angles, and epoch) on their long-term stability over centennial and longer timescales (given in detail in Alessi et al. 2016). We briefly summarize our findings from this extensive numerical experiment, as they pertain to Galileo, and show, based on our recent studies of the dynamical structure of MEO (Daquin et al. 2016), why such general recommendations and guidelines should be taken with a grain of salt. We then tailor our results on the resonant and chaotic structures of the phase space near lunisolar secular resonances (Rosengren et al. 2015; Daquin et al. 2016) towards the analysis of the disposal options for Galileo. In this respect, we address many of the questions left open by the purely numerical study of Alessi et al. (2016). We omit on this occasion any mathematical discussion and simply present the main results at which we have arrived.

2 PARAMETRIC STUDY ON TWO DISPOSAL STRATEGIES

2.1 Introduction and experimental setup

Considerable attention is now being devoted to the problem of determining the long-term stability of MEOs. The problem has been especially timely ever since the advent and launch of the European Galileo and the Chinese Beidou constellations. The main physical mechanisms that can lead to substantial variations in eccentricity, thereby affecting the perigee radius, are resonance phenomena associated with the orbital motion of artificial satellites. While the dynamics of MEOs, governed mainly by the inhomogeneous, non-spherical gravitational field of the Earth, is usually only weakly disturbed by lunar and solar gravitational perturbations, for certain initial conditions, appreciable effects can build up through an accumulation over long periods of time. Such lunisolar resonances, which can drastically alter the satellite's orbital lifetime, generally occur when the second harmonic of the Earth's gravitational potential (J_2) causes nodal and apsidal motions that preserve a favourable relative orientation between the orbit and the direction of the disturbing force (q.v. Rosengren et al. 2015, and references therein). There is also another class of resonances that occurs when the satellite's mean motion is commensurable with the Earth's rotation rate, thereby enhancing the perturbing effects of specific tesseral harmonics in the geopotential. These tesseral resonances pervade the MEOs of the navigation satellites and their net effect is to produce small, localized instabilities in the semimajor axis (Ely & Howell 1997).

A proper understanding of the stability characteristics of the two main types of resonances in MEOs is vital for the analysis and design of disposal strategies for the four constellations. This concerns particularly the question as to whether suitable stable orbits exist such that satellites in these graveyards will not interfere with the constellations, or whether strong instabilities exist, whose destabilizing effects manifest themselves on decadal to centennial timescales, that can be exploited to permanently clear this region of space from any future collision hazard. The process of dynamical clearing of resonant orbits is a new paradigm in post-mission disposal (Jenkin & Gick 2005), but has not been hitherto rigorously studied.

Accordingly, an ESA/GSP study was conducted to numerically examine this idea (q.v. Alessi et al. 2016), using an accurate dynamical model accounting for the Earth's gravity field, lunisolar perturbations, and solar radiation pressure (Table 1). Alessi et al. (2016) particularly investigated to what extent the changes in initial parameters of storage orbits can affect the long-term stability of these orbits over long intervals of time. The study was based on integrations of averaged equations of motion, using a semi-analytic model suitable for all dynamical configurations, which has been approved as the reference model for the French Space Operations Act (through the software STELA and its FORTRAN prototype[1]).

An analysis of the historical practices of the Global Navigation Satellite Systems (GNSS) constellations was performed in order to properly define the reference simulation scenario. The nominal initial conditions and values of area-to-mass ratio considered for each disposal strategy are displayed in Table 2. For the graveyard orbit scenario, it is important to ensure that the storage orbits have only small-amplitude orbital deformations over long periods of time so that the inactive satellites cannot cross the orbital region of active GNSS components (and possibly collide). This, in turn, implies that we must minimize the long-term eccentricity growth in order to delay or prevent the penetration of the GNSS altitude shells. Alternatively, for the eccentricity growth scenario, the possibility

[1] Semi-analytic Tool for End of Life Analysis (STELA) can be downloaded from the CNES website: https://logiciels.cnes.fr/content/stela.

Downloaded from https://academic.oup.com/mnras/article/464/4/4063/2527864 by guest on 01 August 2022

Table 1. Gravitational perturbations added to the central part of the geopotential for the numerical stability analysis. Model 4 (which also includes SRP perturbations with Earth shadow effects) is used for the MEM maps of the ESA study and Model 1 for the fast Lyapunov indicator and Lyapunov time stability maps of Section 4.

	Zonal	Tesseral	Lunar	Solar
Model 1	J_2	Not considered	Up to degree 2	Up to degree 2
Model 2	$J_2, J_2^2, J_3, \ldots, J_5$	Not considered	Up to degree 4	Up to degree 3
Model 3	$J_2, J_2^2, J_3, \ldots, J_5$	Up to degree and order 5	Up to degree 4	Up to degree 3
Model 4	$J_2, J_2^2, J_3, \ldots, J_7$	Up to degree and order 5	Up to degree 3	Up to degree 3
Model 5	$J_2, J_2^2, J_3, \ldots, J_7$	Up to degree and order 5	Up to degree 4	Up to degree 3

Table 2. Initial mean orbital elements considered for the disposal orbits of the Galileo constellations, and the corresponding values of area and mass. The difference in semimajor axis Δa with respect to the nominal constellation is also shown.

Disposal strategy	a (km)	Δa (km)	e	i (°)	A (m^2)	m (kg)
Graveyard orbit	30 150	550	0.001	56	9.3	665
Eccentricity growth	28 086	−1514	0.0539	56	9.3	665

of deorbiting satellites was explored by pushing them into unstable phase-space regions that would slowly decrease their perigee distances, leading to a long-term reduction in the combined constellation and intra-graveyard collision risks (Jenkin & Gick 2005).

The numerical investigation consisted of propagating the initial conditions of Table 2 for 200 yr, under dynamical Model 4 in Table 1, for a large variety of initial orientation phase parameters and analysing the maximum eccentricity attained in each case. This maximum-eccentricity method (MEM) provides a straightforward indication of orbital 'stability' and has been used in a number of astronomical contexts (Dvorak et al. 2003; Nagy, Süli & Érdi 2006; Ramos, Correa-Otto & Beaugé 2015). Instinctively and historically, we expect that the orbits become more unstable as their eccentricities grow; yet, we note that this method is not necessarily an estimator of chaos and stability (since large amplitude variations of eccentricity could be due to regular motion, e.g. secular perturbations, and small oscillations could be the result of slow manifestations of chaotic behaviours, e.g. orbits with large Lyapunov times). Each initial point of the parameter plane was characterized by their maximum eccentricity value (or a closely related quantity) under the following initial conditions (Alessi et al. 2016):

(i) 36 equally spaced values of $\omega \in [0^\circ : 360^\circ]$;
(ii) 36 equally spaced values of $\Omega \in [0^\circ : 360^\circ]$;
(iii) 38 equally spaced initial epochs, starting from $t_0 = 1998$ February 26 (a solar eclipse epoch) to $t_f = 2$ Saros, where Saros indicates a period of 6585.321 347 d.

The same analysis was performed by increasing and decreasing, respectively, the initial inclination by 1° with respect to the nominal value, mainly to account for launch dispersions, but also to understand the neighbouring phase-space regions. Indeed, the aim was not only to see if the known resonant harmonic $2\omega + \Omega$ is actually the most significant, as suggested by many (Chao 2000; Jenkin & Gick 2005; Sanchez et al. 2015; Stefanelli & Metris 2015; to name but a few[2]), but also to gain an insight into the role of the initial inclination and of the Earth–Moon–Sun dynamical configuration on the long-term evolution of the orbits.

[2] See Rosengren et al. (2015) for a detailed literature review on the MEO stability problem.

2.2 Simulation results and discussion

We present here only a subset of the results as the full scope of the study was given in Alessi et al. (2016), and its relation to the other navigation constellations was formulated there more completely. No space will be devoted therefore to any comparison between the similar, albeit less systematic, efforts to tackle this problem by other groups of researchers (e.g. Radtke et al. 2015; Sanchez et al. 2015).

Fig. 1 shows a sample of results from the numerical experiment, and Fig. 2 outlines an 'ω-targeting' strategy to achieve the desired outcome. Similar MEM maps were made for each eclipse year, and the variations in inclination and semimajor axis were tracked in addition to the eccentricity, from which we can restate, from Alessi et al. (2016), the following general observations. The semimajor axis does not change significantly in 200 yr (at most 70 km in absolute value) in any of the cases explored. Consequently, to avoid interferences with the operational constellation, the eccentricity should not exceed 0.02. The minimum eccentricity required to re-enter the atmosphere, assumed to occur whenever the altitude reaches at least 120 km, is about 0.76.

For the graveyard orbit scenario, the eccentricity can reach roughly 0.4 for any of the considered initial inclinations, which depends in a complicated fashion on the various phase angles. We note the vertical bands of stability (negligible eccentricity growth) in (Ω, ω), Fig. 1, that shift as a function of t_0 (not shown here). In general, it was nearly always possible to target an argument of perigee ensuring 'stability' (Fig. 2); that is, for any given (t_0, Ω), there exists at least one initial ω corresponding to a safe disposal. The situation appears more favourable if the initial inclination is increased by 1°, in the sense that the stable vertical bands are wider. Regarding the inclination evolution itself, its behaviour is organized in nearly constant Ω bands in the Ω–ω plane, which also shift in accordance with t_0 (see Alessi et al. 2016, for more details). While the inclination was found to sweep across a relatively large range (between 49° and 63°), no correlation was established with the eccentricity evolution from this study.

Concerning the eccentricity growth scenario, the eccentricity can increase up to 0.8 for the three initial values of inclination considered. The maps, moreover, were found to be periodic in t_0 over a lunar nodal cycle (∼18.61 yr) and nearly symmetric about $\omega = 180^\circ$ (the former holds good in the graveyard scenario as well). In the nominal Galileo case, the eccentricity growth is remarkable in the

Downloaded from https://academic.oup.com/mnras/article/464/4/4063/2527864 by guest on 01 August 2022

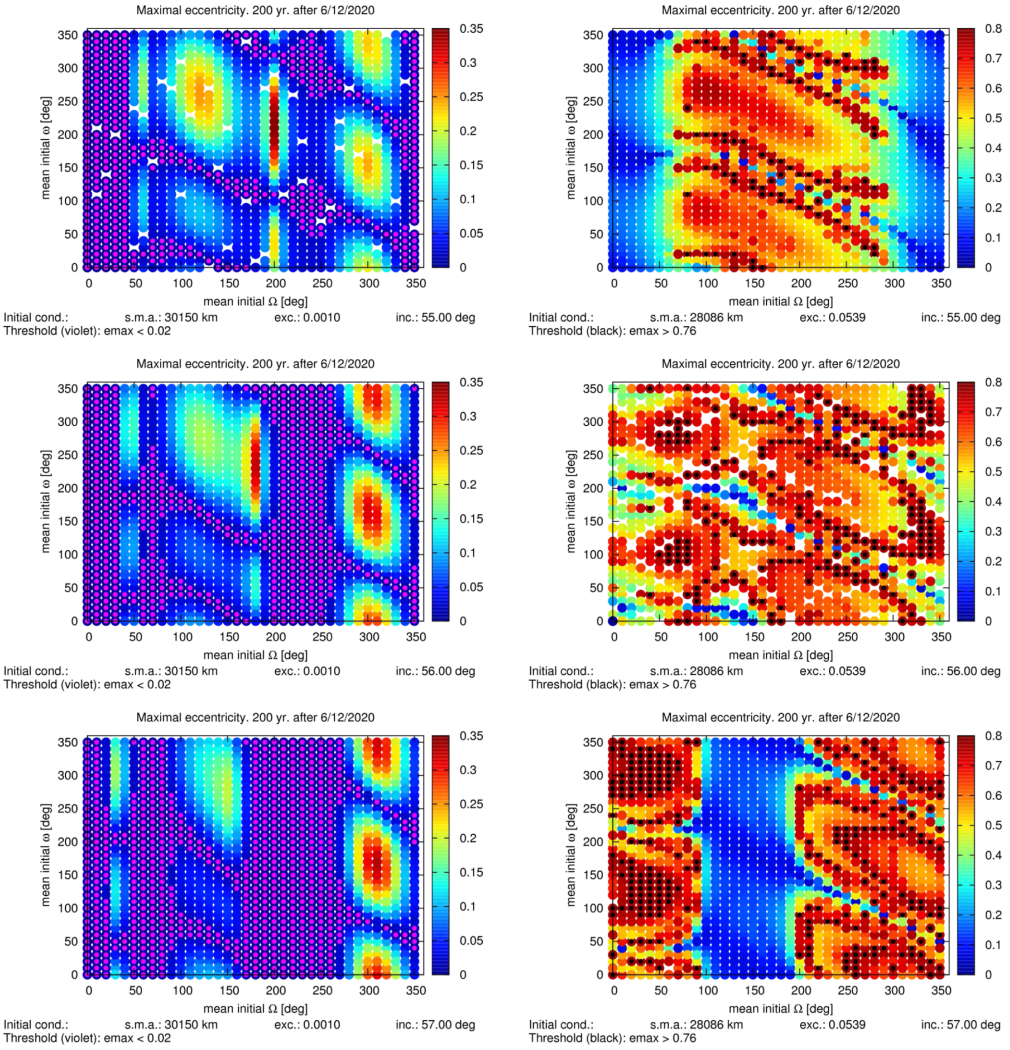

Figure 1. The maximum eccentricity attained in 200 yr (colour bar), as a function of the initial longitude of ascending node and argument of perigee, at a given epoch, for the graveyard orbit (left-hand column) and eccentricity growth (right-hand column) scenarios. Points that meet the various thresholds are indicated by violet ($e_{\max} < 0.02$) and black ($e_{\max} > 0.76$), respectively, and the empty white spaces are locations where data are missing due to numerical issues. Top row: initial inclination decreased by 1°; middle row: nominal initial inclination ($i_0 = 56°$); and bottom row: initial inclination increased by 1°.

entire (t_0, Ω, ω) phase space; specifically, for any given epoch and ascending node, there exists always one (but generally more) initial ω leading to a re-entry (Fig. 2). In the $-1°$ case, re-entry values for e can be achieved if $\Omega \in [50°, 300°]$, whereas in the $+1°$ case, the Ω range depends on t_0. If the satellite's node does not match such values, then the eccentricity tends to stay below 0.1. Regarding the inclination evolution, it was found to sweep through an even greater range of values than in the graveyard scenario, and for the minimum inclination achieved to be organized into patterns in the (Ω-ω) phase plane. While these structures were noted to be similar to those in the maximum eccentricity maps, no useful correlations or insights could be gleaned. We note that while atmospheric re-entries were found to occur for the three cases, they require at least 100 yr.

2.2.1 Practical implications of chaos

Any initial uncertainty in our knowledge of a chaotic system will have small consequences early but profound consequences late, often being rapidly amplified in time. While it is true that the verification of some criteria of stability to define the initial parameters of storage orbits requires long-term orbit propagation up to more than 100 yr, most international recommendations and numerical studies seem fixated on 200-yr forecasts. The 200-yr timespan for future projections is not only arbitrary, but somewhat non-sensical from a dynamical perspective. Every distinct problem in orbital dynamics conditions its own particular scheme of computation, and the question of an appropriate timescale upon which to investigate cannot therefore be answered in a general manner; the answer depends largely on the problem in question and on the degree of knowledge aimed at. An improper assessment can lead to erroneous conclusions regarding stability and chaos. Consider, for example, one of the declared 'safe' graveyard orbits of Fig. 1, as shown in Fig. 3. This orbit does not manifest any significant eccentricity growth for 200 yr, and yet is revealed by our stability analysis (Section 4) to be chaotic with a Lyapunov time of 55 yr. Alternatively, chaotic orbits that initially appear to re-enter (Fig. 3b) may follow evolutionary paths that lead to long-lasting eccentric orbits (Fig. 3d). Note that in Fig. 3(b), the differences between the various models (i.e. mismodelling effects) were too small to affect any appreciable change

Downloaded from https://academic.oup.com/mnras/article/464/4/4063/2527864 by guest on 01 August 2022

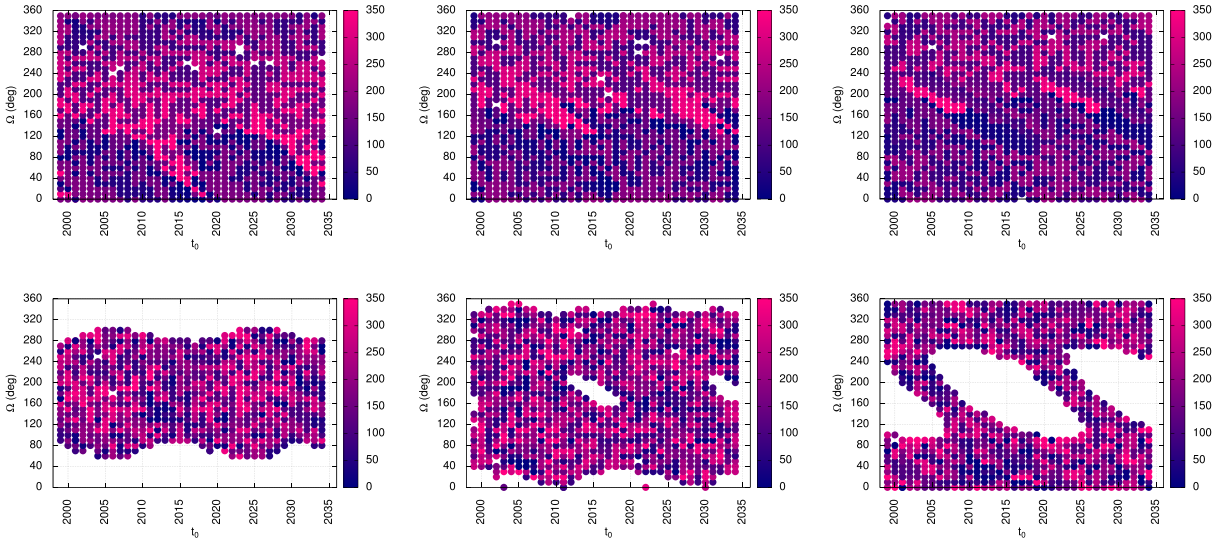

Figure 2. The ω-targeting strategy: the value of argument of perigee (colour bar) that ensures that the eccentricity will not exceed 0.02 in 200 yr (top row) or that ensures a re-entry (bottom row), as a function of the initial epoch and longitude of ascending node. Left-hand column: initial inclination decreased by 1°; middle column: nominal initial inclination; and right-hand column: initial inclination increased by 1°. Empty white spaces indicate locations where the disposal conditions could not be met.

in the time evolutions, over 126 yr integration; yet, a 0.1 per cent change in the initial state can have a significant impact, as shown in Fig. 3(d).

3 RESONANCE OVERLAP AND THE ORIGIN OF CHAOS

3.1 Background

Resonances are regions in the phase space of a dynamical system in which the frequencies of some angular variables become nearly commensurate. Such regions have a profound effect on the long-term dynamics of the system, giving rise to a rich spectrum of highly complicated behaviours (Lichtenberg & Lieberman 1992). It is of great practical importance to understand the mechanisms behind these features, both qualitatively and quantitatively. Recently, it has been realized that lunisolar secular resonances (i.e. those caused by the Moon and the Sun on long timescales) are of particular importance in the MEO regime (Rosengren et al. 2015; Daquin et al. 2016; Celletti et al. 2016b). We review in this section our investigations on the detection of regular structures and chaotic behaviours in the phase space near the navigation satellites. Studying the long-term effects of lunisolar secular resonances is crucial, not only because we need to understand their stability properties, but also because we would like to know whether they could be used (and how) for eventually deorbiting satellites, by forcing them to slowly drift towards high eccentricities and different inclinations.

Despite the variety and complexity of the nature of the dynamics near resonances, we can build an initial intuitive understanding using the mechanics of a pendulum. Pendulum-like behaviour is fundamental to the mathematics of resonance: phase-space structure, separatrices of a periodic motion, and stability (Murray & Holman 2001). The principal effect of the interaction of two resonances is to produce qualitative changes in the separatrix of the perturbed resonance, producing a stochastic layer in its vicinity. The onset of deterministic chaos and the loss of stability is predicted to occur when the separation between the resonances is of the order of their resonance widths (Lichtenberg & Lieberman 1992). Nearly all chaos in the Solar system and beyond has been attributed to the overlapping of resonances (Morbidelli 2002).[3]

3.2 Lunisolar resonant skeleton

Focusing on the MEO region located between three and five Earth radii, namely in a region for which the variation of the argument of perigee ω and longitude of ascending node Ω may be estimated by considering only the effect of J_2 (the second zonal harmonic coefficient of the geopotential) and for which the lunar and solar potentials may be approximated with sufficient accuracy by quadrupole fields, the centre of each lunisolar secular resonance (for prograde orbits) may be approximately defined in the inclination–eccentricity (i–e) phase space by the curves (Rosengren et al. 2015; Daquin et al. 2016)[4]:

$$\mathcal{C}_{\boldsymbol{n}} = \left\{(i,e) \in \left[0, \frac{\pi}{2}\right] \times [0,1] \colon \dot{\psi}_{\boldsymbol{n}} = n_1\dot{\omega} + n_2\dot{\Omega} + n_3\dot{\Omega}_{\rm M} = 0\right\}, \tag{1}$$

for integer coefficients $n_1 \in \{-2,0,2\}$, $n_2 \in \{0,1,2\}$, and $n_3 \in [\![-2,2]\!]$ (not all zero), where

$$\begin{aligned} \dot{\omega}(i,e) &= \frac{3}{4}\frac{J_2R^2\sqrt{\mu}}{a^{7/2}}\frac{5\cos^2 i - 1}{(1-e^2)^2}, \\ \dot{\Omega}(i,e) &= -\frac{3}{2}\frac{J_2R^2\sqrt{\mu}}{a^{7/2}}\frac{\cos i}{(1-e^2)^2}, \\ \dot{\Omega}_{\rm M} &= -0.^{\circ}053\,{\rm d}^{-1}. \end{aligned} \tag{2}$$

[3] Note that while this is the main physical mechanism for the generation of chaos, two overlapping resonances may lead to regular motion sometimes; see for example, Wisdom (1986).

[4] A more accurate location of the resonances, which properly accounts for the equilibrium angle dependencies, can be obtained through a reduced Hamiltonian associated with each resonance.

Downloaded from https://academic.oup.com/mnras/article/464/4/4063/2527864 by guest on 01 August 2022

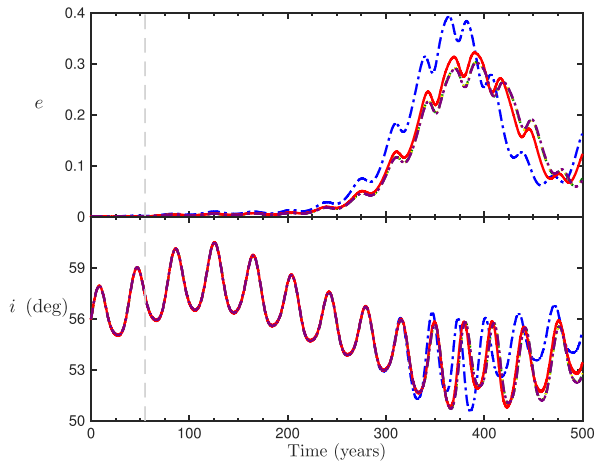

(a) Integrations of a nominally stable disposal orbit under model uncertainties. The solid red line is the evolution from Model 4 in Table 1.

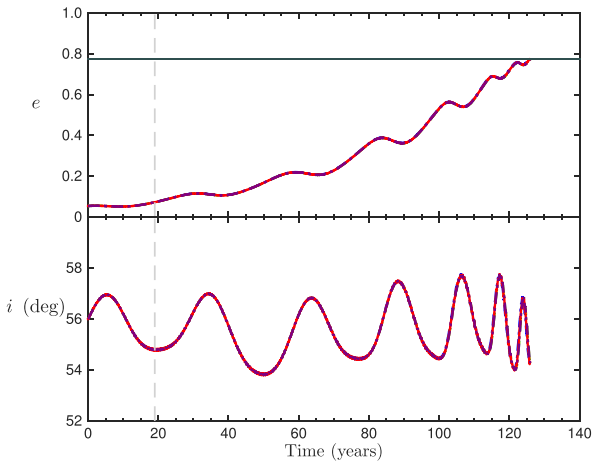

(b) Integrations of the nominal re-entry disposal orbit under model uncertainties. The solid red line is the evolution from Model 4 in Table 1.

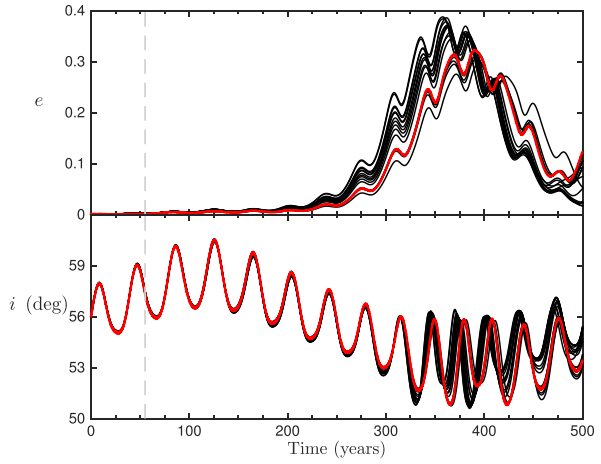

(c) Integrations of 15 nearby orbits of the nominally stable case with random uncertainties of up to 0.1% in a_0, e_0, i_0, Ω_0, ω_0, and $\Omega_M(t_0)$. The thick red line is the nominal orbit of 3(a).

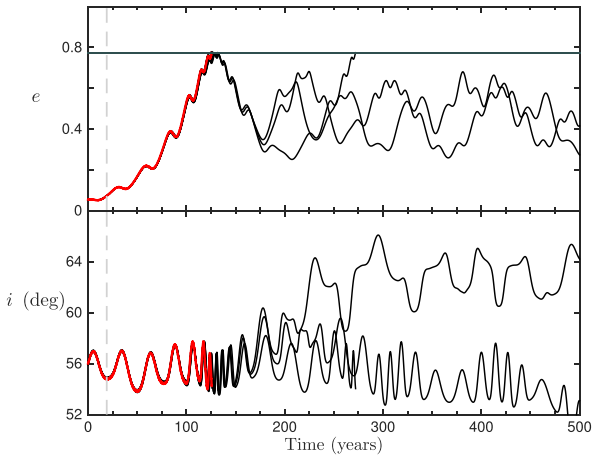

(d) Integrations of 15 nearby orbits of the nominal re-entry case with random uncertainties of up to 0.1% in a_0, e_0, i_0, Ω_0, ω_0, and $\Omega_M(t_0)$. The thick red line is the nominal orbit of 3(b).

Figure 3. Numerical ensemble integrations according to the various dynamical models in Table 1 (top row) and of nearby orbits (bottom row) for apparently safe disposal ($a_0 = 30\,150$ km, $e_0 = 0.001$, $i_0 = 56^\circ$, $\Omega_0 = 70^\circ$, $\omega_0 = 70^\circ$, epoch: 2020 December 6) and re-entry ($a_0 = 28\,086$ km, $e_0 = 0.0539$, $i_0 = 56^\circ$, $\Omega_0 = 60^\circ$, $\omega_0 = 100^\circ$, epoch: 2020 December 6) orbits, wherein the nominal orbits were selected according to Fig. 1. The vertical lines indicate the Lyapunov times, corresponding to an average limit of predictability of each orbit, and the horizontal line indicates the eccentricity value leading to re-entry.

Here the semimajor axis a is a parameter,[5] R is the mean equatorial radius of the Earth, and μ its gravitational parameter. Using the full machinery for pendulums, it can be shown that the curves delimiting the maximum separatrix width of each resonance (i.e. the maximum amplitude inside the libration zone, when each resonance is treated as a pendulum in isolation) are defined by (Daquin et al. 2016)

$$\mathcal{W}_n^{\pm} \equiv \left\{ (i, e) \in \left[0, \frac{\pi}{2}\right] \times [0, 1] \ : \ \dot{\psi}_n = \pm \Delta_n \right\}, \tag{3}$$

in which

$$\Delta_n = 2\sqrt{\frac{3}{2}\frac{J_2 R^2}{a^4}\left|\frac{n_1^2\left(2 - 15\cos^2 i_\star\right) + 10 n_1 n_2 \cos i_\star - n_2^2}{(1 - e_\star^2)^{5/2}} h_n(i_\star, e_\star)\right|}, \tag{4}$$

where h_n is the harmonic coefficient in the lunar and solar disturbing function expansions, associated with the harmonic angle that is in resonance,[6] and $(i_\star, e_\star)$ are the 'actions' at an exact resonance, namely the inclinations and eccentricities that satisfy equation (1).

Fig. 4 shows that resonances fill the phase space near the Galileo constellation. These resonances form in some sense the skeleton or dynamical backbone, organizing and governing the long-term orbital motion. The resulting dynamics can be quite complex, and it has been shown that chaos ensues where resonances overlap (Rosengren et al. 2015; Celletti, Galeş & Pucacco 2016a; Celletti et al. 2016b; Daquin et al. 2016). When such overlapping occurs, only the central part of the resonances, near their elliptic fixed points, might be expected to host regular motion. Chaotic motion can also exist in the vicinity of the perturbed separatrices of isolated resonances, but the absence of overlapping generally guarantees the

[5] The lunar and solar perturbation parameters are proportional to a as $\varepsilon_M = \varepsilon_M(a/a_M)$ and $\varepsilon_S = \varepsilon_S(a/a_S)$; see for example, Celletti et al. (2016b).

[6] Explicit expressions for h_n for each of the 31 distinct curves of secular resonances are given in Daquin et al. (2016).

Downloaded from https://academic.oup.com/mnras/article/464/4/4063/2527864 by guest on 01 August 2022

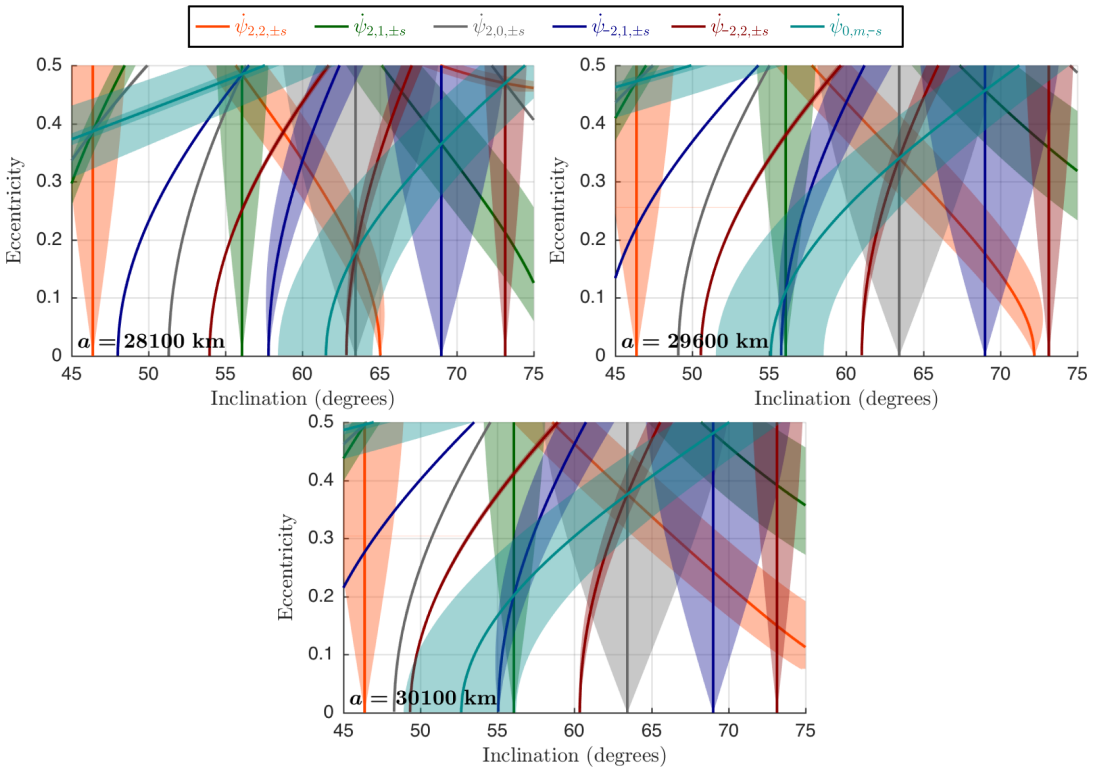

Figure 4. Lunisolar resonance centres $\mathcal{C}_{\boldsymbol{n}}$ (solid lines) and widths $\mathcal{W}_{\boldsymbol{n}}^{\pm}$ (transparent shapes) for various values of the satellite's semimajor axis near Galileo. This plot shows the regions of overlap between distinct resonant harmonics. (Adapted from Daquin et al. 2016, to which we refer for the omitted details.)

local confinement of the motion (Morbidelli 2002; Daquin et al. 2016). It is particularly noteworthy that the nominal inclination of Galileo lies right at the cusp of three distinct and dynamically significant resonant harmonics. Such naivety in the placement of these important assets reflects the need of a real dynamical assessment in constellation design. What is more to the point is that many of the conclusions drawn from the computationally expensive parametric study of Section 2 are easily corroborated here.

There are three principal resonances affecting Galileo-like orbits and their disposal regions: $\dot{\psi}_{2,1,0} = 2\dot{\omega} + \dot{\Omega} \approx 0$, $\dot{\psi}_{-2,1,-1} = -2\dot{\omega} + \dot{\Omega} - \dot{\Omega}_{\rm M} \approx 0$, and $\dot{\psi}_{0,2,-1} = 2\dot{\Omega} - \dot{\Omega}_{\rm M} \approx 0$. In the graveyard orbit scenario, the 55° and nominal inclination cases are more unstable due to the strong interactions of these resonances, whereas increasing the inclination by 1° moves the storage orbits outside of the overlapping regime, naturally leading to a more dynamically stable situation. For the eccentricity growth scenario, the orbits are mainly affected by secular dynamics from the primary $\dot{\psi}_{2,1,0}$ resonance, and the resulting instabilities can be understood from the geometry of this resonance, as discussed in the following section. The phase-portrait topology induced is a resonant libration of the resonant angle, $2\omega + \Omega$, accompanied by a large amplitude oscillation in the eccentricity (Stefanelli & Metris 2015). A small initial eccentricity, built up by this resonance, will increase rapidly once it reaches the overlapping region at about $e = 0.4$. Rather ironically, the targeting of such a low semimajor axis for this disposal strategy appears inappropriate, as keeping the constellation at or near the Galileo semimajor axis would have resulted in similar (if not greater) instabilities with the interaction of the three distinct primary resonances. This basic understanding reached, using pen-and-paper calculations in the manner of Lagrange and Laplace, is a strong testimony to the enduring power of analytical theories in celestial mechanics.

3.3 Disposal criteria based on resonant fixed points

Orbital resonances can be a source of both chaos and stability, the nature of the dynamics depending sensitively on the initial orientation angles of the satellite and the initial lunar node. The asteroid and trans-Neptunian belts of small bodies offer an abundance of instructive examples that illustrate how small zones of stability can persist in the vicinity of resonances, of which the most famous is Pluto (Milani & Nobili 1992; Malhotra 1995). Pluto's orbit is chaotic with a Lyapunov time of about 20 Myr, yet it remains macroscopically stable over billion-year timescales, in the sense that the action variables do not show significant changes. For Pluto, the Kozai–Lidov effect occurs embedded inside a mean-motion resonance with Neptune, giving rise to an argument-of-perihelion libration and a libration of a 3:2 resonant angle, each of which provides a dynamical protection mechanism against close encounters (Malhotra 1995).

The salient feature of a resonance (in the pendulum model) is the existence of an elliptic fixed point, with regular phase-space trajectories encircling it, and of hyperbolic fixed points, connected by a separatrix trajectory. As chaos first develops around the hyperbolic equilibria and separatrices of resonances, their identification should provide a natural definition for the eccentricity growth disposal scenario. Conversely, the elliptic fixed points of the resonances would represent stable phase-space regions for the definition of the graveyard disposal orbits. It must be emphasized that all of the foregoing results and statements hold good only when the resonances admit pendulum-like structures in the phase space, that is, when the associated Hamiltonians can be reduced to the First Fundamental Model of resonance (Breiter 2003). Setting this caveat aside, the small stability islands can also be completely destroyed, depending on the strength of the interaction between resonances. More importantly, the situation is not as clear-cut when treating multiple

Downloaded from https://academic.oup.com/mnras/article/464/4/4063/2527864 by guest on 01 August 2022

Table 3. Lunisolar resonance conditions, harmonic coefficients, and equilibria. Here we use the abbreviations $\mathrm{s} = \sin$, $\mathrm{c} = \cos$, $C = \cos(\epsilon/2)$, and $S = \sin(\epsilon/2)$.

$\dot{\psi}_{\boldsymbol{n}}$	Harmonic coefficient, $h_{\boldsymbol{n}}$	Elliptic	Hyperbolic
$\dot{\psi}_{2,1,0}$	$-\frac{15a^2}{16}\left[\frac{\mu_{\mathrm{M}}(2-3\mathrm{s}^2 i_{\mathrm{M}})CS^{-1}(-2C^4+3C^2-1)}{a_{\mathrm{M}}^3(1-e_{\mathrm{M}}^2)^{3/2}}+\frac{\mu_S \mathrm{s}i_S \mathrm{c}i_S}{a_S^3(1-e_S^2)^{3/2}}\right]e^2\mathrm{s}i(1+\mathrm{c}i)$	$2\omega+\Omega=0$	–
$\dot{\psi}_{-2,1,-1}$	$\frac{15\mu_{\mathrm{M}}a^2\mathrm{s}i_{\mathrm{M}}\mathrm{c}i_{\mathrm{M}}C^2(4C^2-3)}{16a_{\mathrm{M}}^3(1-e_{\mathrm{M}}^2)^{3/2}}e^2\mathrm{s}i(1-\mathrm{c}i)$	$-2\omega+\Omega-\Omega_{\mathrm{M}}=\pm\pi$	$-2\omega+\Omega-\Omega_{\mathrm{M}}=0$
$\dot{\psi}_{0,2,-1}$	$\frac{3\mu_{\mathrm{M}}a^2\mathrm{s}i_{\mathrm{M}}\mathrm{c}i_{\mathrm{M}}C^3S^{-1}(1-C^2)}{8a_{\mathrm{M}}^3(1-e_{\mathrm{M}}^2)^{3/2}}(2+3e^2)\mathrm{s}^2 i$	$2\Omega-\Omega_{\mathrm{M}}=\pm\pi$	$2\Omega-\Omega_{\mathrm{M}}=0$

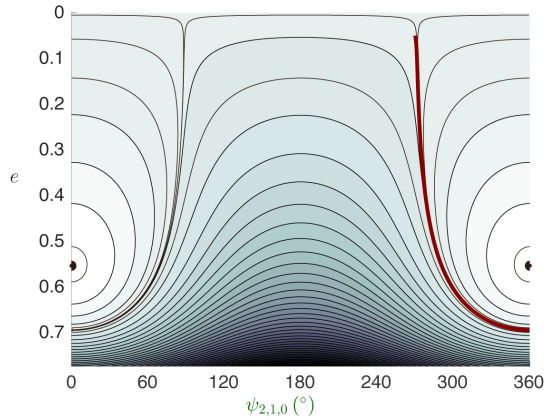

(a) Phase portrait of the $2\dot{\omega}+\dot{\Omega}\approx 0$ resonance for the eccentricity growth case.

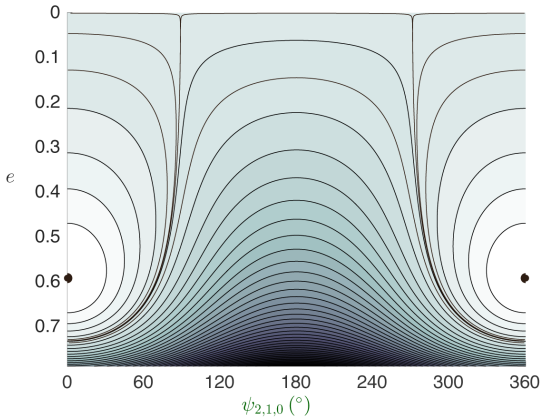

(b) Phase portrait of the $2\dot{\omega}+\dot{\Omega}\approx 0$ resonance for the stable graveyard case.

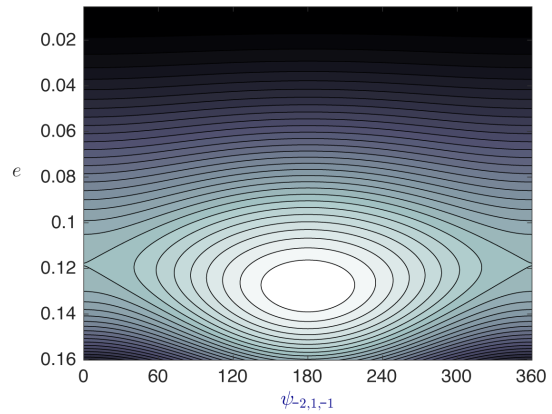

(c) Phase portrait of the $-2\dot{\omega}+\dot{\Omega}-\dot{\Omega}_{\mathrm{M}}\approx 0$ resonance for the stable graveyard case.

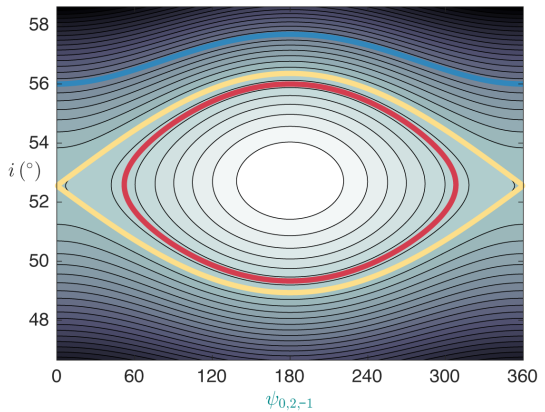

(d) Phase portrait of the $2\dot{\Omega}-\dot{\Omega}_{\mathrm{M}}\approx 0$ resonance for the stable graveyard case.

Figure 5. Phase-plane topology of the three primary resonances affecting Galileo-like orbits and their disposal regions. Panel (a) also features a trajectory starting at $e = 0.05$, $\dot{\psi}_{2,1,0} = 270°$, showing the secular growth from quasi-circular to highly eccentric in 115 yr, resulting from the predominant apsidal resonance. Panel (d) highlights the separatrix of the nodal resonance (yellow) and two trajectories starting at $i = 56°$, but with their phases being, respectively, $\psi_{0,2,-1} = 0$ (blue) and $\psi_{0,2,-1} = 0$ (red).

interacting resonances (as we have here), wherein the geometry of each resonance determines the nature of the dynamics.

We confine the remainder of our discussion to the nominal Galileo inclination 56°, as a similar analysis can be carried out for the other cases. The associated harmonic coefficients and fixed points of the resonances are given in Table 3, and follow from the pendulum-like reduction of Daquin et al. (2016). The phase portraits of each resonance, shown in Fig. 5, depict the interaction between the eccentricity or inclination and the resonant arguments. It is very interesting to note that the $\dot{\psi}_{2,1,0} = 0$ apsidal resonance, for these values of semimajor axes, does not admit the classical pendulum structure (i.e. no hyperbolic equilibria exist) but more closely resembles the Kozai–Lidov resonance (q.v., Morbidelli 2002).[7] While this commensurability is commonly referred to as an

[7] Recent work by Celletti et al. (2016a) and Celletti & Galeş (2016) shows that the 'inclination-dependent-only' resonances, such as $2\dot{\omega}+\dot{\Omega}\approx 0$, exhibit even more complicated phase-space topologies at higher eccentricities, as a bifurcation enters the scene.

Downloaded from https://academic.oup.com/mnras/article/464/4/4063/2527864 by guest on 01 August 2022

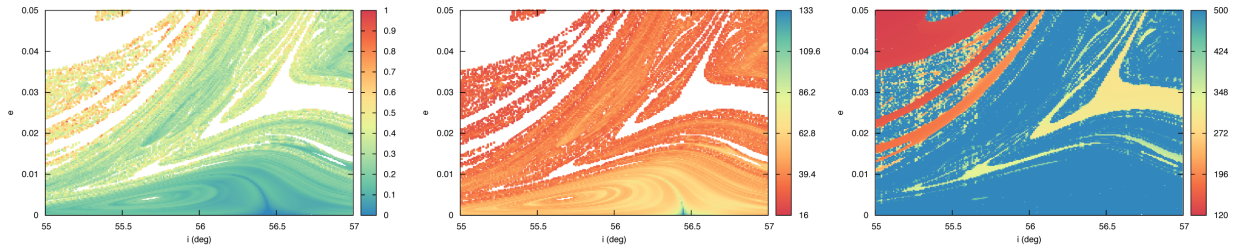

(a) FLI map. (b) Lyapunov time map. (c) Collision time map.

Figure 6. Stability maps characterizing the local hyperbolicity (normalized to 1) and the barrier of predictability (in years) in the vicinity of a proposed graveyard orbit case ($a_0 = 30\,100$ km, $\Omega_0 = \omega_0 = 70^\circ$, epoch: 2020 December 6). The collision time map is provided to illustrate the period of time (in years) after which atmospheric re-entry occurs, and completes the variational maps.

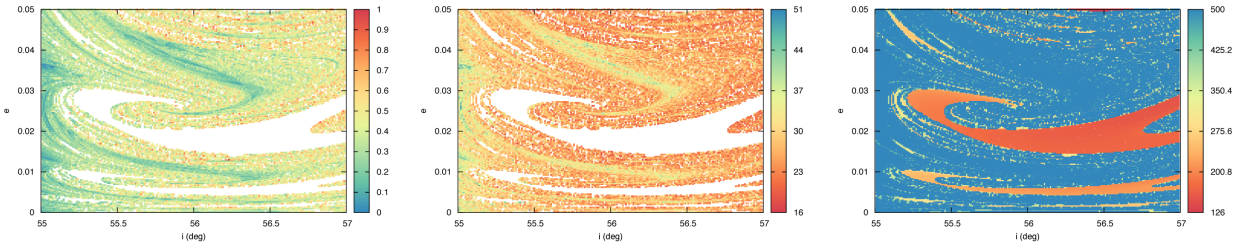

(a) FLI map. (b) Lyapunov time map. (c) Collision time map.

Figure 7. Same as Fig. 6 but for a proposed eccentricity growth case ($a_0 = 28\,100$ km, $\Omega_0 = 60^\circ$, $\omega_0 = 100^\circ$, epoch: 2020 December 6).

inclination-dependent-only resonance (its location being independent of a and e, according to equation (1) and displayed in Fig. 4), this is a serious misnomer. The location of the resonance corresponds to the location of the elliptic fixed point, which, in a proper Hamiltonian treatment, depends on both the eccentricity and the semimajor axis; indeed, in the graveyard orbit case, for $e_\star \approx 0$, $i_\star \approx 53^\circ$, whereas for $e_\star = 0.6$, $i_\star \approx 55^\circ$, the latter equilibrium being depicted in Fig. 5(b). As previously stated, this resonance is responsible for a large-scale secular growth of the eccentricity, but if acting in isolation, it cannot lead to re-entry orbits for the initial conditions in Table 2 (see Fig. 5a, wherein orbits starting at $e = 0.05$ can reach a maximum value of $e \approx 0.7$).

The $\dot{\psi}_{-2,1,-1} = -2\dot{\omega} + \dot{\Omega} - \dot{\Omega}_\mathrm{M} \approx 0$ resonance and the $\dot{\psi}_{0,2,-1} = 2\dot{\Omega} - \dot{\Omega}_\mathrm{M} \approx 0$ nodal resonance both have a pendulum-like structure for the graveyard scenario parameters. The former resonance, however, would only lead to a small-amplitude circulation for the initial elements of the storage orbits, as shown in Fig. 5(c). The nodal resonance by itself, on the other hand, does not directly perturb the eccentricity, but there is a significant indirect perturbation because it can shift the orbits inside or outside of the domain of the primary $\dot{\psi}_{2,1,0} = 0$ resonance, depending on the initial value of the resonant argument (see Figs 4 and 5d). The elliptic and hyperbolic equilibria phase conditions of this resonance thereby lead to simple criteria for the definition of the initial parameters of the disposal orbits: The problem thus reduces to a trivial resonance phase matching scheme, as will be discussed in detail in Section 4.1.

4 NUMERICAL STABILITY ANALYSIS

Fig. 4 gives a crude, global picture of the basic regions in the 2D inclination–eccentricity phase space for which chaotic orbits can be found, and Fig. 5 gives partial information about which initial angles (ω, Ω, and Ω_M) will lead to chaos. To validate this analytical insight, we turn to the numerical detection of chaotic and regular motion through fast Lyapunov indicator (FLI) stability and Lyapunov time maps, which furthermore provide both a global and a local visualization of the curious symbiosis of these two fundamental types of behaviours.

It was shown in Daquin et al. (2016) that Model 1 in Table 1 captures, qualitatively and quantitatively, all of the dynamical structures revealed by the more realistic and more complicated models. We cannot show here how abundant and fruitful the consequences of this realization have proved. The application of this basic physical model leads to simple and convincing explanations of many facts previously incoherent and misunderstood. Here we tailor the recent results of Daquin et al. (2016), to which we refer for omitted details, to the evaluation of the proposed disposal strategies of Alessi et al. (2016) and of our new disposal criteria based on the use of the resonance equilibria and corresponding geometry.

Figs 6 and 7 present several dynamical quantities of interests, in a series of maps,[8] for semimajor axes and parameters near two sample disposal orbits of Section 2: the FLIs (Froeschlé, Guzzo & Lega 2000; Todorović & Novaković 2015), characterizing the degree of hyperbolicity; the Lyapunov time, an estimate of the prediction horizon (Lighthill 1986); and collision time. The FLIs of all regular orbits appear with the same dark blue colour, whereas light blue corresponds to invariant tori, yellow and red to chaotic regions, and white to collision orbits. We find that the volume of collision orbits is roughly the same for the stable and unstable semimajor axes, but that the volume of chaotic obits is indeed larger for the eccentricity growth scenario (where we also find highly unstable and re-entry orbits even for quasi-circular orbits). Inside the collision orbit structures, the re-entry time is nearly constant, and the shortest dynamical lifetime was almost identical in both cases (∼120 yr). For each scenario, the estimated values of the Lyapunov times imply

[8] To produce the various stability maps, the initial conditions were distributed in a regular grid of 200 × 200 resolution, and the model was propagated for 500 yr.

Downloaded from https://academic.oup.com/mnras/article/464/4/4063/2527864 by guest on 01 August 2022

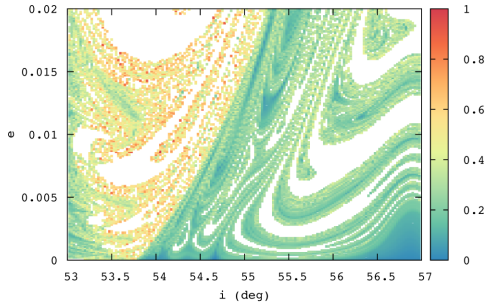

(a) $\Omega = 240^\circ$, $\omega = 30^\circ$, epoch: 2 MAR 1969.

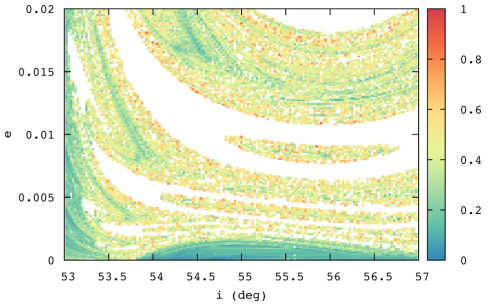

(b) $\Omega = 120^\circ$, $\omega = 120^\circ$, epoch: 2 MAR 1969.

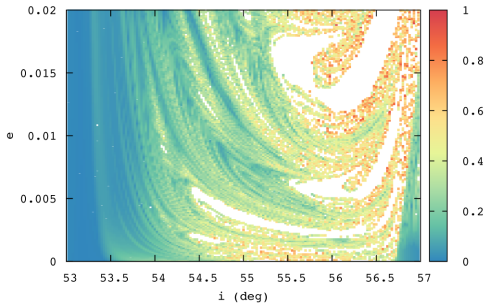

(c) $\Omega = 120^\circ$, $\omega = 120^\circ$, epoch: 23 AUG 1974.

Figure 8. Influence of the initial phases and the initial configuration of the Earth–Moon–Sun system for Galileo's semimajor axis ($a_0 = 29\,600$ km) as a representation of a dynamical system in a lower dimensional phase space.

a very short timescale for reliable predictability, with many orbits having values of the order of only a few decades.

We must stress here that these charts, Figs 6 and 7, have been obtained by varying only the initial inclination and eccentricity, with the initial phases (t_0, Ω, ω) being fixed for all computed FLIs. Fig. 8 shows how the dynamical structures (stable, resonant, chaotic, or collision orbits) evolve by changing the initial phases Ω and ω or even the initial dynamical configuration of the Earth–Moon–Sun system (equivalent to changing the initial epoch). Of course, the FLI maps depend on the choice of initial angles because, as Todorović and Novaković write, '… planes fixed at their different values cross the resonant islands at different positions, and in some special cases the crossing may not even occur. After all, the orbital space is 6D, while our plots are 2D, which certainly gives only a partial insight into the phase-space structure. However, we underline that this does not change the global dynamical pictures of the region, which is essential the same …' Todorović & Novaković (2015). To understand how such features evolve is clearly of remarkable practical application, and will require further study.

We now fix the action-like quantities to their approximate nominal values (Table 2), along with the epoch date, and investigate the geometrical organization and coexistence of chaotic and regular motion in the Ω–ω phase space (Fig. 9). Note the similarity between the MEM maps of Fig. 1 (top row), computed over a 200 yr timespan; yet, the FLI and Lyapunov time maps, besides providing much finer details for the proper detection of invariant structures and chaotic regions, give actual physical information on these unpredictable orbits, whereas the MEM maps provide only one trajectory realization. In the stable case, we again point out how the structures seem to be aligned along vertical bands, and can observe a highly stable region, relatively speaking, near $\Omega = 220^\circ$ (notice how the misleadingly wide bands of stable orbits in Fig. 1 disappear in a proper resolution and computational time). The volume of escaping orbits is larger for the unstable case, and it becomes much more difficult to identify stable regimes. Finally, we note that in both cases, there exists a strong symmetry in the argument of perigee in both maps, which follows naturally from the fact that the secular equations governing quadrupolar gravitational interactions are invariant under the transformation $\omega \mapsto \omega + 180^\circ$ (qq.v., Musen 1961; Tremaine, Touma & Namouni 2009).

From Figs 4 and 5, it is easy to understand how the main resonances organize the global structures in the stability maps of Fig. 9. Recall that the proposed stable graveyard case at $a_0 = 30\,100$ km, $e_0 = 0.001$, and $i_0 = 56^\circ$ is primarily affected by the $\dot{\psi}_{2,1,0} = 2\dot{\omega} + \dot{\Omega} \approx 0$ apsidal resonance and the $\dot{\psi}_{0,2,-1} = 2\dot{\Omega} - \dot{\Omega}_{\rm M} \approx 0$ nodal resonance, though the weaker $\dot{\psi}_{-2,1,-1} = -2\dot{\omega} + \dot{\Omega} - \dot{\Omega}_{\rm M} \approx 0$ resonance is present nearby. We can obtain a partial analytical description of the dynamical structures in the maps through the computed stable and unstable fixed points of the resonances (Table 3). The epoch date determines the initial geometry of the Earth–Moon–Sun system and thus the initial location of the lunar ascending node. Fig. 10 shows the equilibria conditions superimposed on the background FLI maps. The location of the strip of relative stability, apparent only in the graveyard case, is clearly related to the resonant geography of the $\dot{\psi}_{0,2,-1}$ nodal resonance, and the wide vertical band occurs precisely along the line of $\Omega = (2\pi + \Omega_{\rm M})/2$, where $\Omega_{\rm M} \sim 79.^\circ 68$ at the epoch 2020 December 6 UTC. In isolation, this resonance affects only the orbital inclination, and it is clear that its hyperbolic fixed-point phase condition (at 56° inclination) provides a kind of protection mechanism against the large-scale eccentricity transport induced by the $\dot{\psi}_{2,1,0}$ resonance, by keeping its inclination above the domain of the apsidal resonance (cf. Fig. 5d). The elliptic fixed-point condition of this nodal resonance ($2\Omega - \Omega_{\rm M} = \pm\pi$) identifies the approximate location along Ω of the patches of chaotic and collision orbits. In both the graveyard and eccentricity growth cases, the patterns and geometry are aligned along the equilibria curves of the $\dot{\psi}_{2,1,0} = 2\dot{\omega} + \dot{\Omega} \approx 0$ resonance, something crudely pointed out by Sanchez et al. (2015). We should note that any attempt

Downloaded from https://academic.oup.com/mnras/article/464/4/4063/2527864 by guest on 01 August 2022

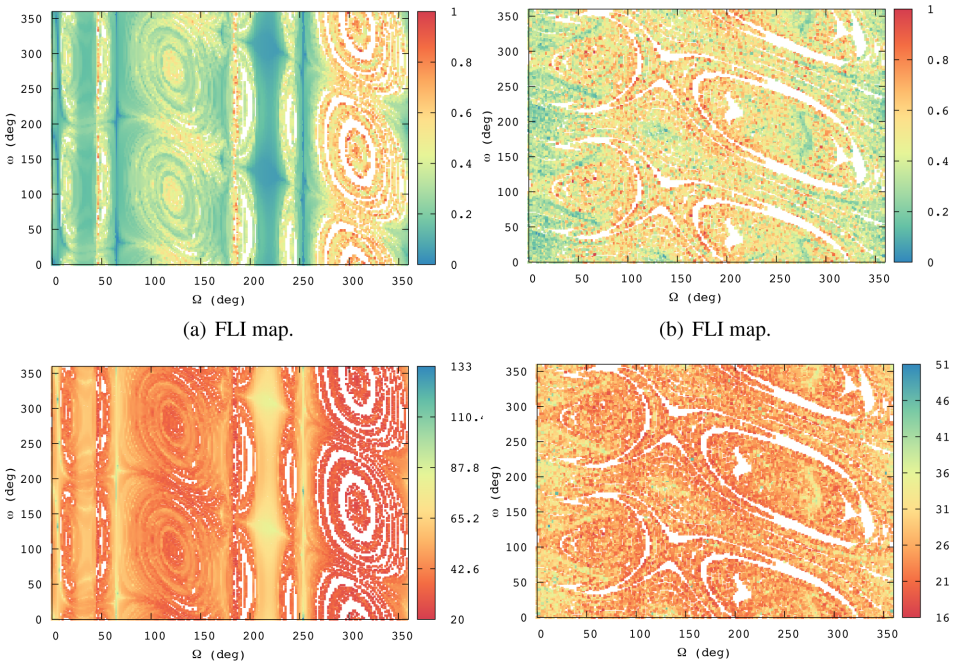

(a) FLI map. (b) FLI map.

(c) Lyapunov time map. (d) Lyapunov time map.

Figure 9. Dynamical structures of the stable (left-hand column: $a_0 = 30\,100$ km, $e_0 = 0.001$, $i_0 = 56^\circ$) and unstable (right-hand column: $a_0 = 28\,100$ km, $e_0 = 0.05$, $i_0 = 56^\circ$) cases in the node–perigee phase space. The colour bar for the FLI maps is normalized to 1 and that for the Lyapunov time maps represents the number of years.

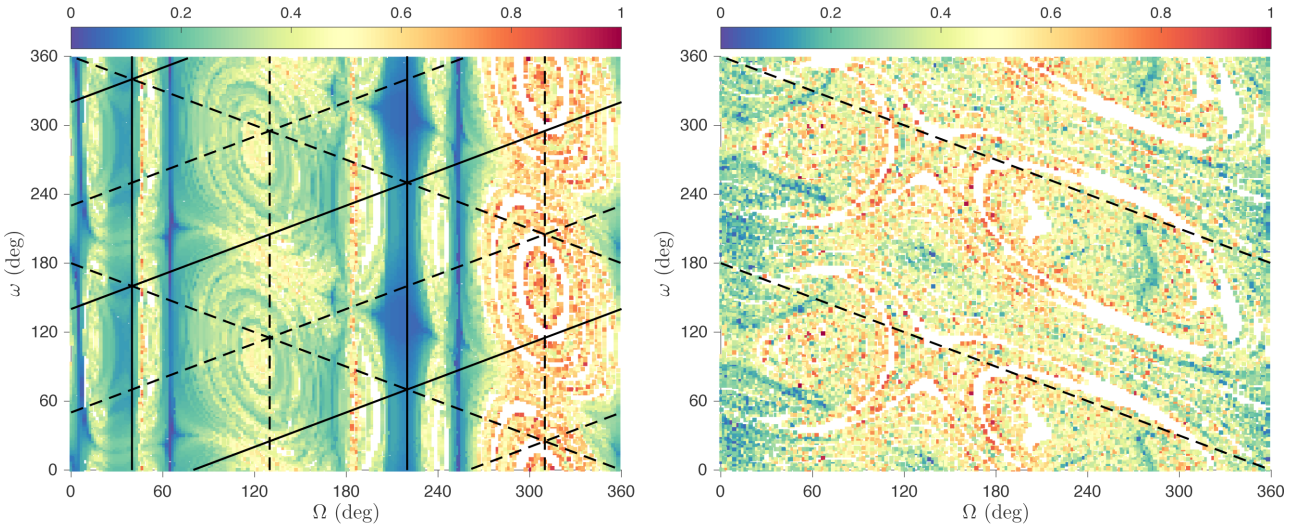

(a) $a_0 = 30\,100$ km, $e_0 = 0.001$, $i_0 = 56^\circ$. (b) $a_0 = 28\,100$ km, $e_0 = 0.05$, $i_0 = 56^\circ$.

Figure 10. Elliptic (dashed lines) and hyperbolic (solid lines) equilibria phase conditions of the relevant resonances of Fig. 4 superimposed on the FLI maps of Fig. 9. The fixed-point lines are defined in Table 3, wherein $\Omega_M = 79.^\circ 68$ for these particular maps.

to describe the phase-space topology induced by the resonances in a rigorous way requires more sophisticated analytical methods that treat resonance interactions; yet, despite this formidable problem, we find that we can still achieve an intuitive understanding through the mathematical study of the resonant equilibria.

Fig. 11 presents the evolution of the FLI maps in the node–perigee phase space, exploring the sensitivity to the initial semimajor axis near the nominal Galileo value. It is particularly noteworthy that the volume of stable orbits is found to increase with increasing semimajor axis, as with the width of the vertical band of stability, occurring near $\Omega = 180^\circ$ (the location of the hyperbolic fixed point phase of the $2\dot{\Omega} - \dot{\Omega}_M \approx 0$ resonance). On the contrary, decreasing the initial semimajor axis from the Galileo constellation, the Ω–ω phase space is nearly globally populated by unstable orbits that surround collisions orbits, the latter organized in pendulum-like structures along the slope defined by the fixed points of the $2\dot{\omega} + \dot{\Omega} \approx 0$ resonance.

4.1 Robustness of the new disposal criteria

In accordance with the results of Fig. 9 that nearly all of the proposed disposal orbits of Section 2 are inherently chaotic with

Downloaded from https://academic.oup.com/mnras/article/464/4/4063/2527864 by guest on 01 August 2022

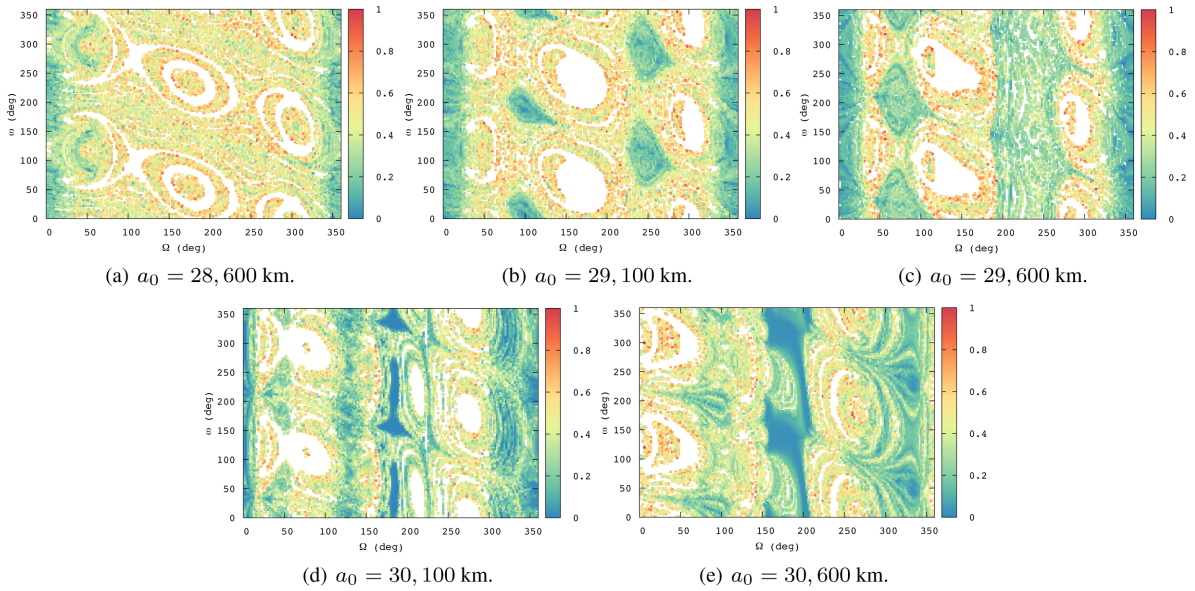

(a) $a_0 = 28,600$ km. (b) $a_0 = 29,100$ km. (c) $a_0 = 29,600$ km.

(d) $a_0 = 30,100$ km. (e) $a_0 = 30,600$ km.

Figure 11. Influence of the strength of the perturbation on the dynamical structures near Galileo's semimajor axis ($e_0 = 0.02$, $i_0 = 56.^\circ1$, epoch: 1969 March 2).

Lyapunov times of the order of decades, the computation of individual trajectories becomes not only impractical, but also irrelevant. The loss of long-time predictability implies that we must abandon the notion of individual orbits and instead focus on ensembles of trajectories. Rather than attempt an approximate, statistical description of the motion through transport theory (q.v., Meiss 1992), we content ourselves here with analysing ensemble integrations only, in order to test the robustness of the resonant geometry disposal scheme.

Given the symmetry in the argument of perigee, we can essentially identify eight general points of interest in Fig. 10(a): the intersection of the equilibrium phase curves of the primary resonances. Fig. 12(a) presents their trajectory realizations over a 500 yr timespan. As expected, the orbits along the hyperbolic equilibria phase of the $2\dot{\Omega} - \dot{\Omega}_{\rm M} \approx 0$ nodal resonance yield more stable evolutions (their inclinations being kept above 56°), whereas those along the elliptic equilibria phase are highly chaotic, some of which are dynamically short-lived (relatively speaking). The orbits located in the vertical band of Fig. 10(a) at $\Omega = 219.^\circ84$ appear to be the most stable, and thus a simple graveyard disposal criterion naturally presents itself, which does not require the strict (and seemingly arbitrary) perigee-targeting scheme of Section 2. The release epoch can be correlated with an initial lunar node, and as the satellite's node naturally precesses due to Earth oblateness perturbations, one must only wait (chalará) for the appropriate lunar-satellite nodal phasing in order to ensure a stable graveyard (i.e. $e < 0.02$ for at least 200 yr), as validated in Figs 12(b) and (c) on an ensemble level. Of course, a perigee and node around this orbit can be selected from the FLI maps themselves to yield an even more stable system (Fig. 12d); yet, even here the orbit eventually succumbs to its chaotic nature. We note that the correlation between the Lyapunov time and an effective stability time is delicate to establish (Milani & Nobili 1992), and should be pursued in future work.

It is probably unreasonable to expect space operators to have detailed FLI stability maps for each epoch or (what amounts to the same thing) initial lunar node. As noted by Alessi et al. (2016), the structures in the MEM maps of Section 2 appear to remain fixed, only shifting with initial epoch. While the same likely holds true for the FLI maps, our proposed graveyard orbit criterion should be tested in the absence of such maps. There is, in this respect, an ambiguity as to which hyperbolic equilibria of the $2\dot{\Omega} - \dot{\Omega}_{\rm M} \approx 0$ nodal resonance will give the wider stability band, if one even exists (cf. Fig. 10, where the two dashed vertical lines are located at $\Omega = 39.^\circ84$ and $\Omega = 219.^\circ84$, respectively); consequently, both should be examined to determine the more stable solution. Fig. 13 shows ensemble integrations of the nodal resonance hyperbolic fixed-point criteria (i.e. $\Omega = (2\pi + \Omega_{\rm M})/2$ or $\Omega = \Omega_{\rm M}/2$), with ω randomly chosen, for a few other epochs that were considered in Alessi et al. (2016). The same analysis was carried out for the remaining 34 initial epochs of that study (which incidentally turned out to sample well the various lunar nodes), from which we can loosely conclude that Fig. 13(b) represents the general behaviour for initial lunar nodes in the ranges $\Omega_{\rm M} \in [0^\circ, 125^\circ]$ and $\Omega_{\rm M} \in [220^\circ, 360^\circ]$, whereas Fig. 13(c) generally corresponds to the evolutions outside of these zones. Fig. 13(a) represents a sort of an extreme behaviour found only in a few cases, wherein the orbits can slightly penetrate the threshold eccentricity ($e > 0.02$) within a 200 yr integration time and even eventually reach Earth-collision orbits. Overall, these results seem to corroborate the lunar-satellite nodal phase scheme for defining stable graveyards for the Galileo constellation. When effected, this strategy generally keeps the eccentricities below 0.02 for at least 200 yr while simultaneously locking the inclination into a long-period oscillation; this inclination behaviour should also contribute to diluting the probability of collisions within the graveyard orbits (q.v., Jenkin & Gick 2005).

The situation is not as clear for the proposed re-entry disposal solution, wherein, for the considered semimajor axis ($a_0 = 28\,100$ km), there exists only the dominant apsidal resonance initially (Figs 4 and 10b), but which interacts with many resonances at higher eccentricities. However, we note from Figs 10(a) and 11 that there exist closer (are even more circular) orbits to the nominal Galileo constellation that can lead to atmospheric re-entry, and whose resonant topology may allow for a better determination of the precise structures in the FLI maps.

Downloaded from https://academic.oup.com/mnras/article/464/4/4063/2527864 by guest on 01 August 2022

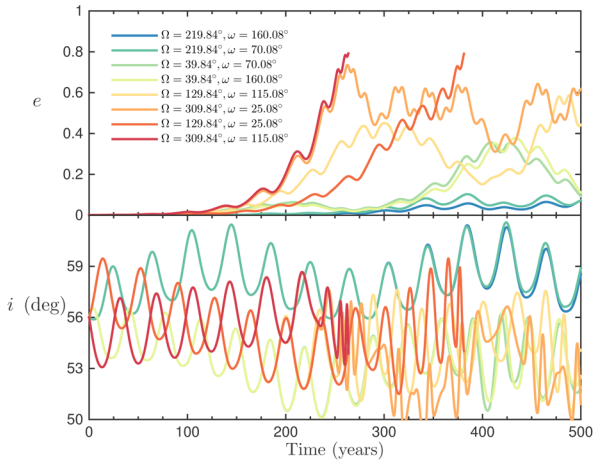

(a) Integrations of the elliptic and hyperbolic fixed point phase conditions of the lunisolar secular resonances near the proposed Galileo graveyard orbit ($a_0 = 30\,100$ km, $e_0 = 0.001$, $i_0 = 56°$).

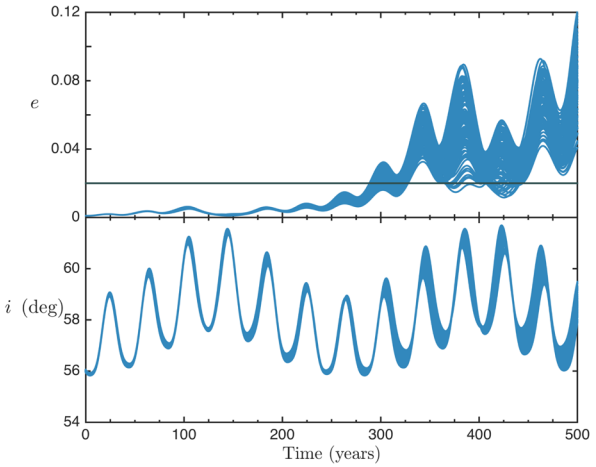

(b) One hundred ensemble integrations of the most *stable* orbit of Fig. 12(a) ($\Omega = 219.84°, \omega = 160.08°$), under the same errors as in Fig. 3(c).

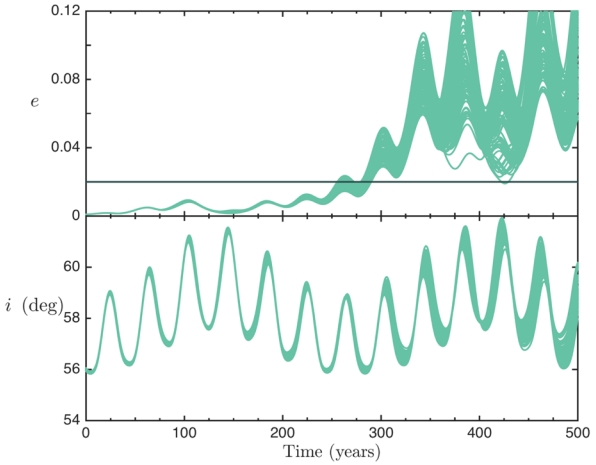

(c) One hundred ensemble integrations of the orbit located at the elliptic fixed point of nodal resonance and hyperbolic fixed points of the apsidal resonances at $\Omega = 219.84°$ and $\omega = 70.08°$, under the same errors as in Fig. 3(c).

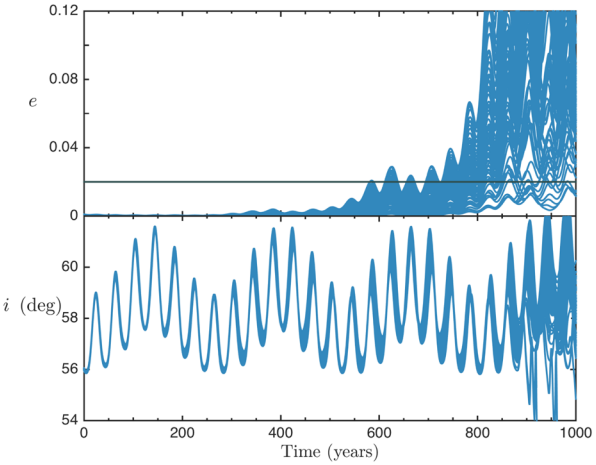

(d) One hundred ensemble integrations of an orbit roughly located in the middle of the stability pocket of the FLI map at $\Omega = 217°$ and $\omega = 130°$, under the same errors as in Fig. 3(c).

Figure 12. Numerical integrations of orbits selected according to the equilibria curves and FLI map of Fig. 10(a) ($a_0 = 30\,150$ km, $e_0 = 0.001$, $i_0 = 56°$, epoch: 2020 December 6).

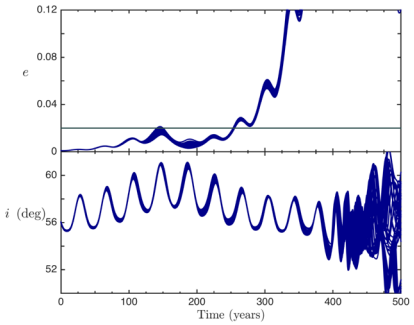

(a) $\Omega_M = 160.56°$ (epoch: 26 FEB 1998), $\Omega = 260.28°, \omega = 139.86°$.

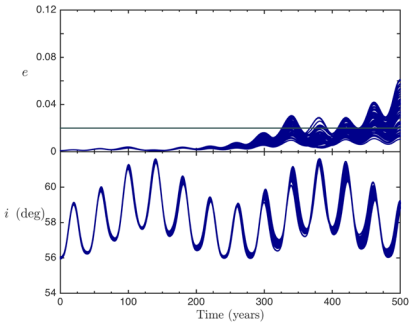

(b) $\Omega_M = 355.28°$ (epoch: 12 SEPT 2006), $\Omega = 177.64°, \omega = 1.18°$.

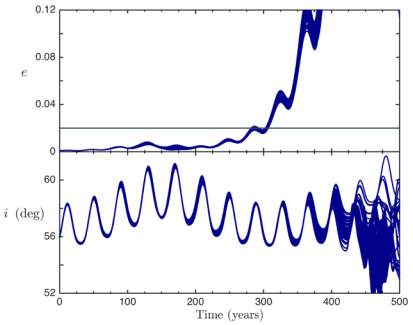

(c) $\Omega_M = 208.17°$ (epoch: 15 APR 2014), $\Omega = 104.08°, \omega = 37.96°$.

Figure 13. 50 ensemble integrations of orbits selected according to the unstable equilibria of the nodal resonance in Table 3 for various disposal epochs ($a_0 = 30\,150$ km, $e_0 = 0.001$, $i_0 = 56°$).

Downloaded from https://academic.oup.com/mnras/article/464/4/4063/2527864 by guest on 01 August 2022

5 CONCLUSION

Sections 1 and 2 may seem to revel overmuch in our past imperfections on the MEO stability problem; yet, it is no longer possible to investigate the motion of celestial bodies without being fully conscious of the possibilities of chaos, a fact now well known to dynamical astronomers. Resonant and chaotic phenomena are ubiquitous in multifrequency systems, and the knowledge of their long-period effects is essential for determining the stability of orbits and the lifetime of satellites. The complexity of the dynamical environment occupied by the Earth's navigation satellites is now becoming clearer (Rosengren et al. 2015; Daquin et al. 2016; Celletti et al. 2016a). Resonant phenomena are widespread within the MEO region as a whole but particularly so amongst the highly inclined orbits of the navigation satellite systems, and a clear picture of the dynamics near these resonances is of considerable practical interest. We can now identify the sources of orbital instability or their absence in the MEO region, and their nature and consequences in the context of long-term dynamical evolution. We examined them in terms of the detection of stability and unstable zones, with a particular view on the choice of the Galileo constellation disposal orbits. This paper links theoretical aspects of resonant and chaotic dynamics to practical applications, and lays an essential logical foundation for future developments.

ACKNOWLEDGEMENTS

Some results of this paper were presented at the 25th International Symposium on Space Flight Dynamics (ISSFD), 2015, Munich, Germany. This paper has benefited, directly or indirectly, from stimulating and useful discussions with S. Breiter, A. Celletti, T.A. Ely, C. Galeş, M. Guzzo, G. Pucacco, D.J. Scheeres, and N. Todorović. We especially thank F. Gachet and I. Gkolias, of the University of Rome Tor Vergata, for their technical contributions to this paper and for specific conversations about the disposal criteria. Many of the numerical stability map simulations were hosted at CNES, for which we are particularly grateful. This work was partially funded by the European Commissions Framework Programme 7, FP7-PEOPLE-2012-ITN (Grant Agreement 317185). JD acknowledges the partial financial support from the Australian Research Council project (ID LP130100243).

REFERENCES

Alessi E. M., Deleflie F., Rosengren A. J., Rossi A., Valsecchi G. B., Daquin J., Merz K., 2016, Celest. Mech. Dyn. Astron., 125, 71
Barrow J. D., 2010, in Bryson B., ed., Seeing Further: The Story of Science, Discovery, and the Genius of the Royal Society. Harper Press, London, p. 360
Breiter S., 2003, Celest. Mech. Dyn. Astron., 85, 209
Brouwer D., 1959, AJ, 64, 378
Celletti A., Galeş C., 2016, Frontiers Astron. Space Sci., 3, 11
Celletti A., Galeş C., Pucacco G., 2016a, SIAM J. Appl. Dyn. Syst., 15, 1352
Celletti A., Galeş C., Pucacco G., Rosengren A. J., 2016b, Celest. Mech. Dyn. Astron. Available at: http://link.springer.com/article/10.1007%2Fs10569-016-9726-8
Chao C. C., 2000, Adv. Astronaut. Sci., 105, 817
Daquin J., Rosengren A. J., Alessi E. M., Deleflie F., Valsecchi G. B., Rossi A., 2016, Celest. Mech. Dyn. Astron., 124, 335
Dvorak R., Pilat-Lohinger E., Funk B., Freistette F., 2003, A&A, 398, L1
Ely T. A., Howell K. C., 1997, Int. J. Dyn. Stab. Syst., 12, 243
Froeschlé C., Guzzo M., Lega E., 2000, Science, 289, 2108
Jenkin A. B., Gick R. A., 2005, in Danesy D., ed., Proc. 4th European Conf. Space Debris ESA SP-587: Dilution of Disposal Orbit Collision Risk for the Medium Earth Orbit Constellations. ESA/ESOC, Darmstadt, Germany, p. 309
Laskar J., Gastineau M., 2009, Nature, 495, 817
Lichtenberg A. J., Lieberman M. A., 1992, Regular and Chaotic Dynamics, 2nd edn. Springer-Verlag, New York
Lighthill J., 1986, Proc. R. Soc. A, 407, 35
Malhotra R., 1995, AJ, 110, 420
Meiss J. D., 1992, Rev. Mod. Phys., 64, 795
Milani A., Nobili A. M., 1992, Nature, 6379, 569
Morbidelli A., 2002, Modern Celestial Mechanics: Aspects of Solar System Dynamics. Taylor & Francis, London
Murray N., Holman M., 2001, Nature, 410, 773
Musen P., 1961, J. Geophys. Res., 66, 2797
Nagy I., Süli Á., Érdi B., 2006, MNRAS, 370, L19
Radtke J., Domínguez-González R., Flegel S. K., Sánchez-Ortiz N., Merz K., 2015, Adv. Space Res., 56, 2626
Ramos X. S., Correa-Otto J. A., Beaugé C., 2015, Celest. Mech. Dyn. Astron., 123, 453
Rosengren A. J., Alessi E. M., Rossi A., Valsecchi G. B., 2015, MNRAS, 449, 3522
Sanchez D. M., Yokoyama T., Prado A. F. B. A., 2015, Math. Probl. Eng., 2015, 382340
Stefanelli L., Metris G., 2015, Adv. Space Res., 55, 1855
Todorović N., Novaković B., 2015, MNRAS, 451, 1637
Tremaine S., Touma J., Namouni F., 2009, AJ, 137, 3706
Wisdom J., 1986, Celest. Mech., 38, 175
Zeebe R. E., 2015, ApJ, 811, 9

This paper has been typeset from a TEX/LATEX file prepared by the author.

Downloaded from https://academic.oup.com/mnras/article/464/4/4063/2527864 by guest on 01 August 2022